

1 **Fast quantification of nanorod geometry by DMA-spICP-MS**

2 Jiaojie Tan^{1,2}, Yong Yang², Hind El Hadri¹, Mingdong Li³, Vincent A. Hackley^{*1}, and Michael R.
3 Zachariah^{*2,3}

- 4 1. Materials Measurement Science Division, National Institute of Standards and Technology,
5 Gaithersburg, Maryland 20899, United States
6 2. University of Maryland, College Park, Maryland 20742, United States.
7 3. Chemical Sciences Division, National Institute of Standards and Technology, Gaithersburg,
8 Maryland 20899, United States

9 **Abstract**

11 A fast, quantitative method for determining the dimensions of nanorods (i.e., length and diameter)
12 is described, based on hyphenation of differential mobility analysis (DMA) with single particle
13 inductively coupled plasma mass spectrometry (spICP-MS). Seven gold nanorod samples with
14 different dimensions (diameters 11.8 nm to 38.2 nm, aspect ratios 1.8 to 6.9) were used to validate
15 the method. We demonstrate that DMA-spICP-MS can (1) achieve quantification of both length
16 and diameter comparable with TEM analysis, (2) make statistically meaningful measurements in
17 minutes at low concentrations ($< 10^8/\text{mL}$) and (3) separate nanorods from spheres and quantify the
18 geometry of each population. A robustness analysis of this method was performed to evaluate
19 potential biases in this approach.

20 **Introduction**

22 Rod-shaped metallic nanoparticles (nanorods) are increasingly applied in across a range of fields
23 including biomedicine, catalysis and electronics [¹⁻⁵]. In particular, gold nanorods (GNRs) have
24 been used in diagnostics,^[6] biosensors,^[7] and hyperthermal therapy^[8], due to their size-dependent
25 localized surface plasmon resonance (SPR). Rod-shaped metal oxides, such as Fe₃O₄, CeO₂, TiO₂
26 and others have been employed as catalysts or essential components for heterogeneous catalysis
27 applications.^[1] The critical dimensions (i.e., length and diameter) of the rod are crucial in
28 determining the properties of interest, and can influence final utilization. Therefore, the control of
29 dimensions during synthesis and post-synthesis requires rapid and reliable analytical tools, which
30 are currently scarce beyond imaging approaches.

31 Transmission electron microscopy (TEM) is the most frequently used method to obtain dimensions
32 of nanorods; however, a sufficiently large number of particles, N , must be counted to obtain
33 statistically reliable results (i.e., measurement precision increases in proportion to \sqrt{N}), which can
34 be costly and laborious. Furthermore, artifacts such as aggregation can be produced during sample
35 preparation and can complicate image analysis.

36 Efforts have also been made to relate GNR dimensions to unique spectral features. [⁹⁻¹³]. For
37 instance, Link et al. [⁹] modeled the optical absorption spectra of GNRs and derived a simple
38 relationship between the longitudinal SPR (LSPR) absorption maximum and the aspect ratio (AR).
39 The extraction of geometric parameters is primarily based on electromagnetic modeling and with

40 the assistance of *a priori* knowledge of mean diameter and end shape. [14-16] Hu et al. [17]
41 developed a more convenient method from spectral fitting by establishing LSPR relations for
42 GNRs, and achieved reliable results. However, such simulations require significant expertise in
43 the fundamental theories and therefore are not widely available to non-experts. Applications are
44 limited to well-defined GNRs, and are not readily extendable to non-SPR associated nanorods,
45 such as hybrid metal rods or metal oxides. This approach becomes considerably more complex
46 and less accurate when dealing with a mixture of geometries or length/diameter distributions.

47 In prior work [18, 19] we have employed ion-mobility methods coupled to inductively coupled
48 plasma mass spectrometry (ICP-MS). The differential mobility analyzer (DMA) is a type of ion-
49 mobility spectrometer that classifies particles based on mobility size in the range from 2 nm to
50 hundreds of nm. Depending on the operational conditions, a DMA can achieve a resolution up to
51 100:1 (capable of differentiating a 1 % difference in mobility). [20] The DMA can also be used as
52 a band pass filter to select one specific mobility size, which can be passed to another instrument
53 or detector. Theories investigating ion mobility of non-spherical nanoparticles have been
54 extensively studied. [21] For cylindrical shaped particles in particular, the exact analytical
55 expression of mobility depends on two geometric parameters, diameter and length (d_r and L_r).
56 Zachariah and coworkers [22, 23], for example, developed a pulsed DMA to obtain geometry
57 information by systematically changing the alignment of nanorods using a varying electric field to
58 vary mobility. This method, however, requires the nanorods to be conductive in order to align in
59 the applied field.

60 Single particle ICP-MS (spICP-MS) is an emerging technique with the capability of
61 simultaneously determining both the concentration and mass of metal nanoparticles. In comparison
62 to traditional ICP-MS, spICP-MS utilizes very fast acquisition times (μs) to capture single particle
63 events, and therefore is capable of characterization on a “particle by particle” basis. Each particle
64 is presented as an ion-mass resolved intensity directly proportional to the mass of the particle
65 ionized in the plasma. For a cylindrical shaped particle, mass is a function of d_r and L_r , so
66 combining the independent information from mobility (i.e., derived from DMA measurement)
67 with mass (i.e., derived from spICP-MS), d_r and L_r are theoretically calculable and can be
68 performed in a single hyphenated measurement. An analogous, though off-line approach, was
69 explored by Nguyen et al., [24] where fractions from a polydisperse commercial GNR sample were
70 collected following separation by asymmetric flow field-flow fractionation. Off-line analysis of
71 fractions was performed using spICP-MS to extract length; the diameter was obtained from
72 independent TEM imaging and assumed constant in this study (GNRs were grown from the same
73 seed size).

74 We have previously explored tandem analysis with DMA and spICP-MS for simultaneous and
75 accurate measurement of size, mass and concentration, and validation using NIST Au nanoparticle
76 reference materials.[19, 25] In this proof-of-principle study, we extend our previous work to non-
77 spherical particles and the simultaneous characterization of GNR diameter and length, while
78 demonstrating the capacity to obtain statistically meaningful measurements in minutes at very low
79 particle concentrations (10^5 to 10^8)/mL. Finally, we use this hyphenated approach to distinguish
80 nanorod populations from spherical/non-nanorod impurities in a mixture, a measurement critical
81 for manufacturing quality control.

82

83 **Experimental**

84 **Materials**

85 Cetyltrimethylammonium bromide (CTAB) stabilized GNRs in aqueous suspension were obtained
86 from Nanopartz (Loveland, CO, USA)[†] and citrate stabilized GNRs were obtained from
87 NanoComposix (San Diego, CA, USA). LSPR bands for the GNRs range from 600 nm to 1400
88 nm. The naming scheme presented in Table 1 indicates the surface coating and the LSPR. For
89 example, CIT-660 refers to citrate capped GNRs with LSPR at 660 nm. There are two GNR
90 samples with LSPR at 850 nm, but they differ in diameter (20 nm and 40 nm). To distinguish
91 between these two, we included their diameters in the sample name: *viz.* CTAB-20-850 and
92 CTAB-40-850.

93
94 NIST Reference Material 8013 (RM8013, Gold Nanoparticles, Nominal 60 nm Diameter) was
95 used as a calibration standard for spICP-MS. NIST RM8012 (Gold Nanoparticles, Nominal 30 nm
96 Diameter) was used with RM8013 as representative spherical gold particles. Ammonium acetate
97 (99.9 %, Sigma-Aldrich, St. Louis, MO, USA) was added to solutions as a volatile electrolyte for
98 the electrospray process to generate charged aerosols from aqueous suspensions. GNR samples
99 were first diluted in ammonium acetate to the desired concentration just prior to analysis. Electron
100 microscopy grids (carbon and lacey carbon films) were purchased from Ted Pella (Redding, CA,
101 USA).

102 103 **Instrumentation**

104 **TEM**

105 Transmission electron microscopy (TEM) was performed using a JEOL-2100 FEG (JEOL,
106 Peabody, MA) with an accelerating voltage of 200 kV. To obtain the geometries of GNRs (Table
107 1), each aqueous GNR sample was drop-cast onto a carbon coated TEM grid. To examine the
108 surface coating of GNRs after electrospray treatment, GNRs were selected at the peak mobility
109 using the DMA as a bandpass filter, and directly deposited electrostatically onto a lacey carbon
110 film for TEM imaging. Nanometer Aerosol Sampler (model 3089, TSI Inc., Shoreview, MN) was
111 used for electrostatic deposition.

112 **DMA-spICPMS hyphenation**

113 GNRs were introduced to the DMA (model 3081, TSI Inc., Shoreview, MN, USA) by electrospray
114 (ES) (model 3480, TSI Inc.) operated with a differential pressure of 2.6×10^4 Pa (3.7 psi) and
115 using a 40 μ m fused silica capillary. The DMA was operated with a sheath flow of argon at 10
116 L/min, and an aerosol flow of air at 1 L/min. The voltage applied to the power supply was
117 controlled by an in-house LabVIEW software program (version 10.0.1, National Instruments,
118 Austin, TX). The DMA step size was 2 nm with a step dwell time of 31 s. The ICP-MS (7700x,
119 Agilent Technologies, Santa Clara, CA, USA) was operated in time resolved single particle mode
120 with a dwell time of 10 ms. Online gas phase hyphenation of DMA to ICP-MS was achieved by a
121 gas exchange device (GED) connected by silicone conductive tubing throughout the system. The
122 GED was utilized to solve the incompatibility of air in the plasma. A gas exchange efficiency of
123 about 90 % was achieved with a sweep flow of 4 L/min through the gas exchange device. For a
124 more detailed description of the setup and operation, refer to our previous publication.^[19]

125

126 **Method**127 **Basis of ES-DMA-spICP-MS in quantifying GNR dimensions**

128 Particle mobility size is commonly expressed as an equivalent spherical diameter, (i.e., electrical
 129 mobility diameter) regardless of the actual particle shape. Electrical mobility diameter represents
 130 the diameter of a sphere that has the equivalent mobility of the analyte. For a spherical particle,
 131 the electrical mobility diameter is equivalent to its geometric diameter. However, for non-spherical
 132 particles, the measured electrical mobility diameter is a function of both particle shape and particle
 133 orientation during transit through the DMA. For simplicity, our model was built on the assumption
 134 that the GNR is a cylindrical shape with flat end-caps defined by two geometrical parameters: *viz.*
 135 diameter (d_r) and length (L_r). Although orientation of GNRs can be subject to factors such as sheath
 136 flow and aspect ratio, in addition to the applied electrical field, by operating at low voltage (i.e.,
 137 $< 2\text{kV}$), fully random orientation is achieved. [26,27] The capacity for ES-DMA-spICP-MS
 138 hyphenation to determine d_r and L_r relies on the fact that it provides simultaneous characterization
 139 of mobility diameter, $d_{m,r}$, from DMA and mass, m_r , (or volume, v_r , if density is known) from
 140 spICP-MS ^{197}Au intensity. In this case, $d_{m,r}$, m_r , d_r and L_r are related as follows (see also Figure S1
 141 in the Electronic Supplementary Information, ESI):[28]

$$142 \quad d_{m,r} = ((d_r + \Delta d_{gas})(L_r + \Delta d_{gas}) + \frac{1}{2}(d_r + \Delta d_{gas})^2)^{\frac{1}{2}}; \quad (1)$$

$$143 \quad I_r \propto m_r = \rho v_r = \rho \left(\pi \left(\frac{d_r}{2} \right)^2 L_r \right); \quad (2)$$

144 where I_r is the ICP-MS event intensity generated by a GNR of mass m_r . The two equations ((1)
 145 and (2)) yield two unknowns (d_r , L_r), and are therefore solvable. It is worth mentioning that the
 146 original model also added the finite diameter of the gas molecule (Δd_{gas}) to the geometry of rod.
 147 [23,29] Therefore, we added Δd_{gas} to both d_r and L_r , where inclusion of Δd_{gas} significantly improves
 148 the accuracy of the mobility model. In this case, $\Delta d_{gas} = 2 \times 0.34 \text{ nm}$.

149 The least squares method was used to search for the optimal combination of d_r and L_r , such that
 150 the calculated $d_{m,r}$ and v_r from Eq. (1)-(2) yield the best fit to the measured $d_{m,r,0}$ and $v_{r,0}$.
 151 Mathematically,

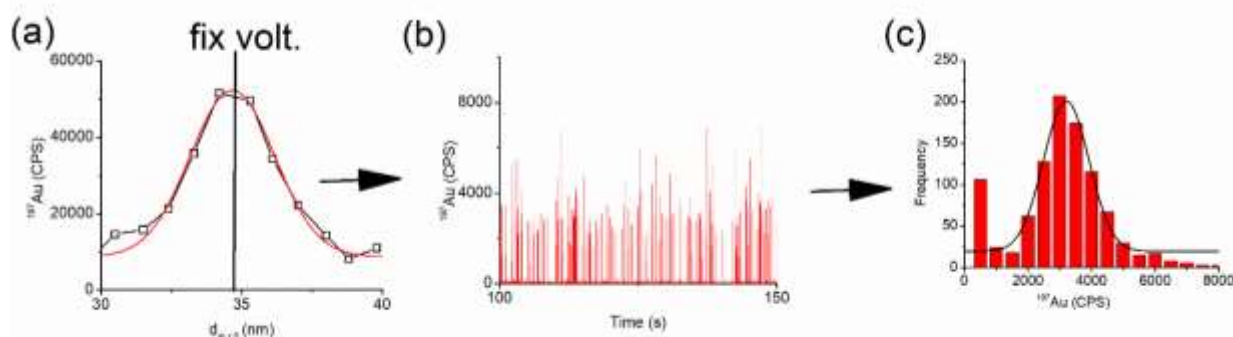
$$152 \quad \left(\frac{v_r - v_{r,0}}{v_{r,0}} \right)^2 + \left(\frac{d_{m,r} - d_{m,r,0}}{d_{m,r,0}} \right)^2 == \text{minimum} . \quad (3)$$

153

154 **Procedure**

155 For each GNR sample, the mass-weighted mobility size distribution was determined by DMA-
 156 ICP-MS in non-single particle mode (Figure 1(a)). The sample was then diluted to an appropriate
 157 concentration for spICP-MS measurement (i.e., from $10^5/\text{mL}$ to $10^8/\text{mL}$). For example, the
 158 estimated concentration was $4 \times 10^8/\text{mL}$ for CTAB-600 and $3.3 \times 10^8/\text{mL}$ for CTAB-40-850. The
 159 limit of detection for the DMA-spICP-MS in terms of concentration and mass was described in
 160 our previous work. [19] GNRs selected at the peak mobility diameter ($d_{m,r}$) are representative of
 161 the central tendency of the population. Experimentally, the DMA was set at a specific voltage

162 (previously determined) corresponding to the peak mobility, for an observation time, t , during
 163 which the ICP-MS was operating in time-resolved single particle mode to detect single GNR
 164 events. Figure 1 (b) shows the raw spectrum for the spICP-MS signal, each spike representing one
 165 GNR event. A standard 5σ criteria was used to distinguish particle events from the background.
 166 [30] The intensity of each spike was then converted to a frequency histogram (Figure 1(c)) to obtain
 167 the mean intensity by Gaussian fit. With appropriate calibration by reference material (NIST
 168 RM8013), the mean intensity was then converted to the mean mass (or volume, v_r) for a single
 169 GNR event. For this we calculated the mass (or volume, v_r) of RM8013 based on the reference
 170 TEM mean diameter with assumed spherical geometry. This in turn yields the volume per unit
 171 intensity and was utilized to obtain the volume of the GNR based on mean intensity from Figure
 172 1(c). Finally, $d_{m,r}$ and v_r were fit to the experimental values $d_{m,r,0}$ and $v_{r,0}$ using the least squares
 173 method (i.e., Eq. (3)) to obtain d_r and L_r .



174
 175 Figure 1. Procedure to determine mobility diameter ($d_{m,r,0}$) and volume ($v_{r,0}$) by DMA-spICP-MS method.
 176 (a) Intensity (volume) based mobility size distribution by DMA-ICP-MS (ICP-MS operates in non-single
 177 particle mode ($t_{dwell} = 0.5$ s), ^{197}Au in counts per second (CPS) was reported). Peak maximum represents the
 178 $d_{m,r,0}$ of the central tendency of the GNR population. For samples diluted to appropriate concentration, DMA
 179 was set at a voltage corresponding to the peak $d_{m,r,0}$. GNRs corresponding to this voltage were then delivered
 180 to the ICP-MS operated in single particle mode ($t_{dwell} = 10$ ms). (b) spICP-MS events for GNRs selected at
 181 peak $d_{m,r,0}$. (c) Intensity distribution for (b). Peak of the Gaussian fit to histogram in (c) was used as the
 182 mean intensity to calculate v_r .

183

184 Results and Discussion

185 Characterization of GNRs by TEM

186 A representative wide range of GNR dimensions were selected in order to validate the DMA-
 187 spICP-MS method. These dimensions include d_r (11.8 nm to 38.2 nm), L_r (47.1 nm to 151.7 nm)
 188 and AR (2 to 6.9). The surface coating and suspending medium for GNRs were reported by the
 189 vendor. The dimensions d_r and L_r were independently determined by TEM. Roughly 200 GNRs
 190 were measured for each population, with the population means and standard deviations
 191 summarized in Table 1. Representative TEM images are provided in the electronic supplementary
 192 information (ESI, Figure S2). Vendor provided d_r and L_r are also provided in the ESI (Table S1)
 193 for comparison. The relatively larger uncertainty associated with CTAB-1400 is attributed to
 194 instability / alteration in GNR size over time, since the 200 GNRs were collected and imaged at

195 two time points over a year apart. All other samples exhibited consistency / stable geometry within
 196 this same time frame.

197 Table 1. Characterization of GNRs by TEM

GNRs	Dimeter (d_r, nm)	Length (L_r, nm)	Aspect Ratio (AR)	Surface / Medium
CIT-660	17.5±1.2	47.1±6.7	2.7±0.5	Citrate / Water
CIT-800	11.9±1.3	51.4±5.3	4.3±0.6	Citrate / Water
CIT-980	11.8±1.1	70.4±9.2	6.1±1.2	Citrate / Water
CTAB-600	30.9±4.6	56.4±7.4	1.8±0.2	CTAB/3mmol/L CTAB
CTAB-20-850	20.7±1.4	89.6±12.8	4.3±0.6	CTAB/3mmol/L CTAB
CTAB-40-850	38.2±4.2	135.4±12.7	3.6±0.5	CTAB/3mmol/L CTAB
CTAB-1400	24.6±7.2	151.7±54.1	6.9±3.7	CTAB/5mmol/L CTAB

198

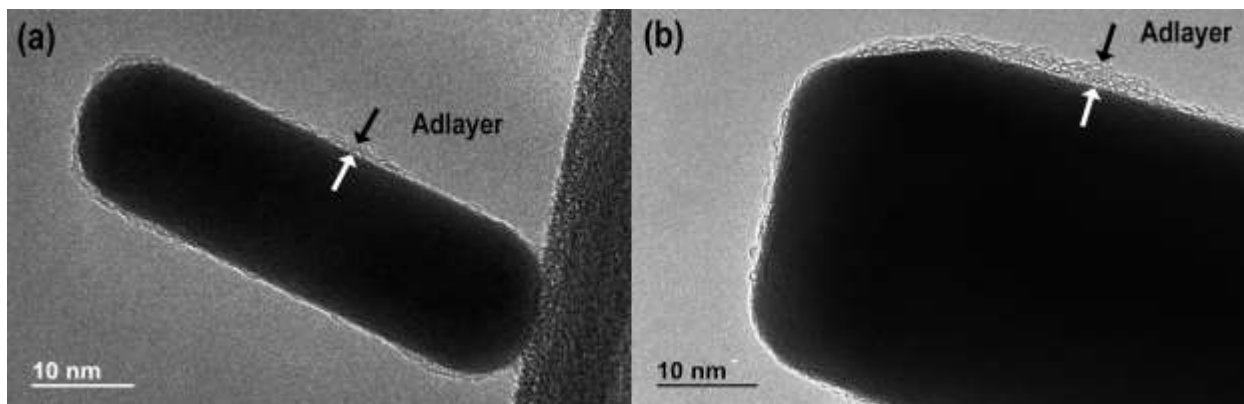
199

200 TEM evaluation of surface coating

201 TEM images clearly show a thin relatively low-electron-density adlayer on the GNRs (Figure 2).
 202 This coating is persistent across the majority of GNRs imaged, though occasionally it is not visible
 203 or the thickness is not uniform - it varies slightly across individual GNRs, even within the same
 204 sample. GNRs used in this study are either citrate or CTAB coated. The medium is deionized water
 205 or 3 mmol/L or 5 mmol/L aqueous CTAB. In addition to the native coating, non-volatiles (e.g.,
 206 CTAB, salts) in the medium will dry onto the GNR surface during the ES process. The total dried
 207 coating thickness should be included for a complete mobility model (Eq. (1)). To sample enough
 208 GNRs for image-based analysis of the surface coating, GNRs were collected at native
 209 concentration and at the peak mobility using DMA as a band filter; however, DMA-spICP-MS
 210 measurements on these samples were, out of necessity, performed at much lower concentrations.
 211 To confirm that dilution does not significantly affect the adlayer thickness, the difference in
 212 adlayer thickness on GNRs at the native concentration and at 60× dilution was evaluated for
 213 CTAB-1400; the difference proved to be negligibly small (see Figure S3 in ESI). Based on this
 214 result, it is reasonable to assume that sampling at the native concentration is sufficiently
 215 representative of GNR coatings under conditions used for DMA-spICP-MS analysis. Mean values
 216 were obtained to estimate the thickness used in subsequent calculations (see Figure S4 (a)-(b) in
 217 ESI). Additionally, the singular contribution from non-volatiles was estimated independently
 218 based on the non-volatile peak measured by ES-DMA using a condensation particle counter (see
 219 Figure S5 in ESI).

220 Finally, we incorporate the thickness of the coating adlayer (Δd_{layer}) into Eq. (1) to obtain a
 221 complete mobility model:

$$222 \quad d_{m,r} = ((d_r + \Delta d_{gas} + \Delta d_{layer})(L_r + \Delta d_{gas} + \Delta d_{layer}) + \frac{1}{2}(d_r + \Delta d_{gas} + \Delta d_{layer})^2)^{\frac{1}{2}} \quad (4)$$



223
 224 Figure 2. Two representative TEM images show evidence for a thin low density adlayer on the surface of
 225 GNRs. Both citrate and CTAB coatings were examined: (a) CIT-660 (b) CTAB-40-850

226

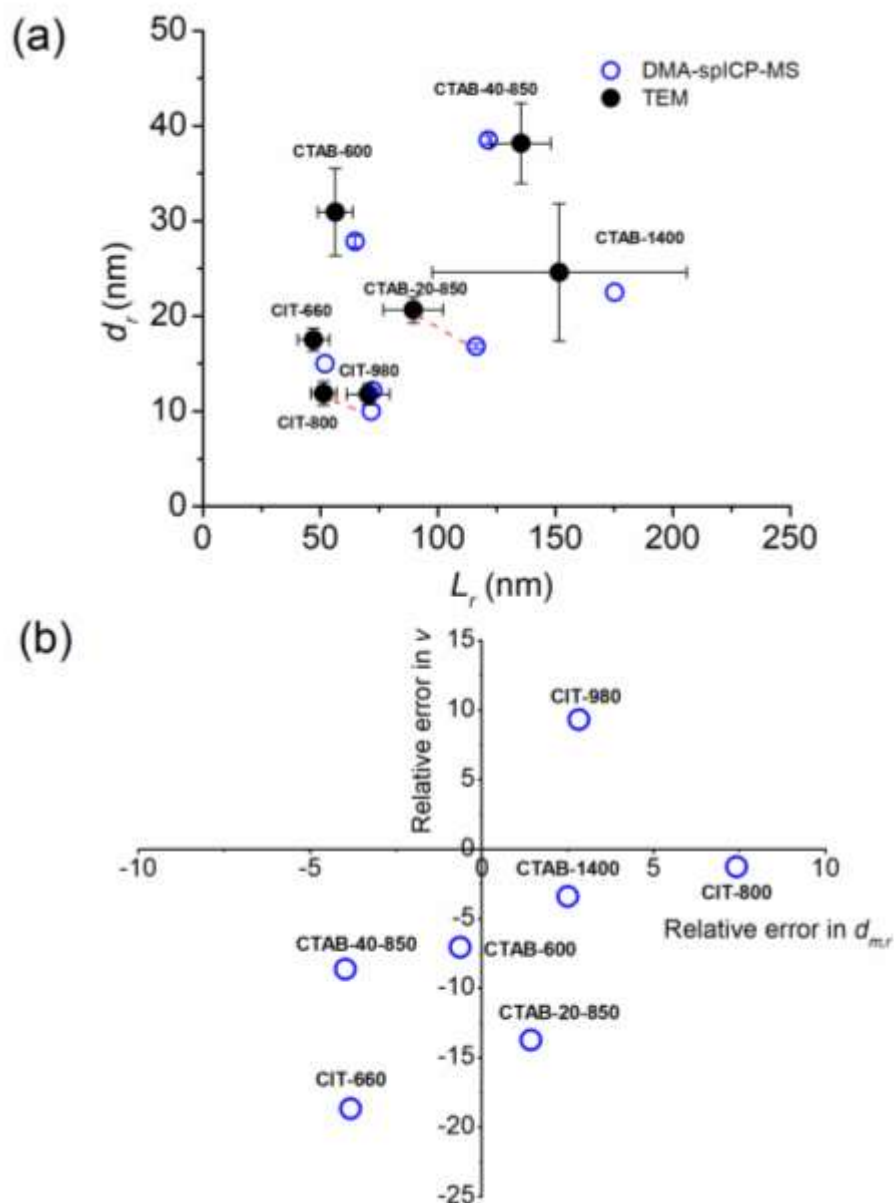
227 Accuracy of DMA-spICP-MS for quantitative GNR dimensions

228 The seven GNR samples listed in Table 1 were analyzed by DMA-spICP-MS, and the d_r and L_r
 229 were compared (see Figure 3(a)) with values directly obtained by TEM (which is used here as a
 230 benchmark). Overall, the values are consistent and comparable. Not surprisingly, the accuracy of
 231 d_r and L_r (obtained by DMA-spICP-MS) relies strongly on the accuracy of the measured $d_{m,r,0}$ and
 232 $v_{r,0}$ (in eqn (3)). Using Eq. (1) and (2), v and $d_{m,r}$ were calculated based on d_r and L_r obtained
 233 directly from TEM (Δd_{layer} and Δd_{gas} were added to the calculation in Eq.(1)). The measured $d_{m,r}$,
 234 and v by DMA-spICP-MS was then compared with this calculated (benchmark) value and the
 235 difference reported as relative error.

$$236 \quad \text{relative error} = \frac{(d_{m,r} \text{ by DMA-spICP-MS}) - (d_{m,r} \text{ calculation based on TEM})}{d_{m,r} \text{ calculation based on TEM}} \%$$

237 The same definition was used for calculation of relative error in v . In Figure 3(b), for most of the
 238 GNRs examined, both $d_{m,r}$ and v measurements fell within a 10 % relative error range. CIT-660
 239 and CTAB-20-850, have a relatively larger deviation in v than the other GNRs with -19 % and -
 240 14 % respectively. Another important observation is that, even though the errors in ($d_{m,r}$, v) are
 241 comparable ((7%, -1%), (3%, 9%), (-4%, -9%)) for CIT-800, CIT-980, CTAB-40-850,
 242 respectively (Figure 3(b)), the prediction of d_r and L_r based on Figure 3(a) for CIT-800 deviated
 243 from the TEM result to a larger extent (39 % in L_r and -16 % in d_r) in comparison to the other
 244 materials (e.g., CIT-980 (3 % in L_r , and 3 % in d_r), CTAB-40-850 (-10 % in L_r and 1 % in d_r)).
 245 This suggests that sensitivity of the model (robustness) to error in $d_{m,r}$ and v measurements may
 246 differ significantly based on GNR dimensions. This also suggests that the weight or importance
 247 of error in $d_{m,r}$ and v measurement might differ in their influence upon the final accuracy of the
 248 prediction of L_r and d_r . A detailed robustness analysis discussing this phenomenon is presented
 249 in the following section. It is worth noting that, despite this result, for most GNRs, d_r and L_r lie
 250 well within the one standard deviation range of TEM results (error bars represent 1σ). The
 251 relatively large error bars from TEM (average of roughly 200 GNRs) indicates the polydisperse
 252 nature of the GNR samples. It should be emphasized that the DMA-spICP-MS method described
 253 here measures the dimensions of the population central tendency and therefore has a negligible
 254 polydispersity. Finally, it is interesting to note that there is a noticeable trend for DMA-sp-ICP-

255 MS estimates to be smaller in diameter and larger in length compare with TEM. This might
 256 indicate a bias or systematic error of unknown origin. Though the statistical sampling is too
 257 small to support any finite conclusion here, it merits further scrutiny in future work.



258
 259 Figure 3. (a) Comparing d_r and L_r determined by DMA-spICP-MS (open circles) to that obtained
 260 by TEM (solid circles). Red dash lines connect data points corresponding to the same sample, in
 261 cases where the relationship may not be clear. Error bars represent one standard deviation (3
 262 replicate measurements for DMA-spICP-MS and roughly 200 GNRs for TEM). If error bars are
 263 not visible, they are smaller than the symbol. (b) Relative error (%) in $d_{m,r}$ and v measured by
 264 DMA-spICP-MS in comparison to theoretical calculation based on TEM.

265

266

267 **Robustness analysis**

268 To test the method robustness, the effect of perturbation (bias or error) in each parameter (i.e., $d_{m,r}$,
269 v and Δd_{layer}) on the final predicted d_r and L_r was evaluated. The $d_{m,r}$, v and Δd_{layer} based on TEM
270 measurements were used as benchmarks (zero point of x-axis in Figure 4) for quantifying the
271 extent of perturbation. When examining the perturbation of one parameter, e.g. $d_{m,r}$, the other
272 parameters (v and Δd_{layer}) were kept at the benchmark value. A +5 % perturbation in $d_{m,r}$ is $1.05\times$
273 benchmark $d_{m,r}$, while -5 % is $0.95\times$ the benchmark value. All three parameters were then applied
274 to our model to predict d_r and L_r . The final combined error (CE) in comparison to actual d_r and L_r
275 in TEM was used as a quantitative metric for the method and is mathematically defined as:

$$276 \quad CE = \left(\left(\frac{d_r - d_{r,0}}{d_{r,0}} \right)^2 + \left(\frac{L_r - L_{r,0}}{L_{r,0}} \right)^2 \right)^{\frac{1}{2}} \quad (5)$$

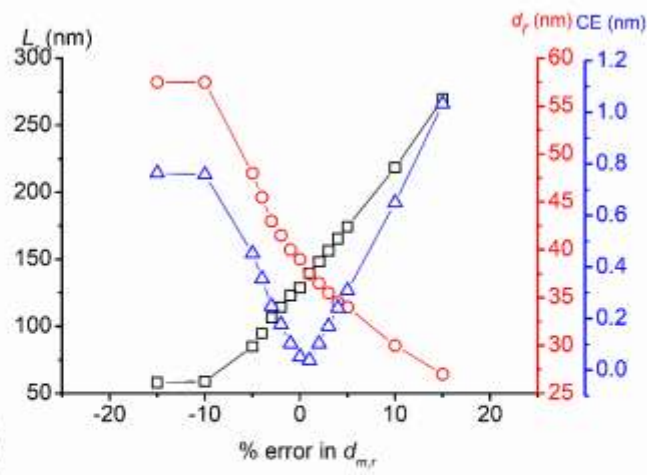
277 Where $d_{r,0}$ and $L_{r,0}$ is the benchmark TEM diameter and length of GNRs. From the definition of
278 CE, $CE/2$ represents the average error in prediction of d_r or L_r .

279 Figure 4(a) presents the change of predicted d_r , L_r and CE as a function of $d_{m,r}$ perturbation. Note
280 that d_r and L_r change in the opposite direction (red and black trace) with respect to perturbation in
281 $d_{m,r}$, while there is a minimum (valley) for CE (blue trace).

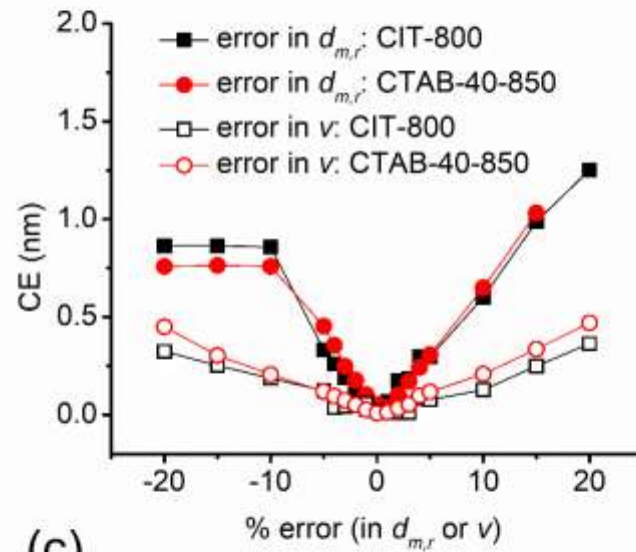
282 Next we evaluated the effect of perturbation in $d_{m,r}$ and v , using two GNRs with substantially
283 different dimensions (CIT-800 with d_r of 11.9 nm and L_r of 51.4 nm, and CTAB-40-850 with d_r
284 of 38.2 nm and L_r of 135.4 nm). In Figure 4(b), for the same percentage of perturbation in both
285 $d_{m,r}$ and v , the latter yields a much lower final CE for the two GNRs considered. In other words, v
286 is more resistant to perturbation in measurement compared to $d_{m,r}$, and explains why CIT-800
287 exhibits the largest deviation in d_r and L_r prediction, as it has the largest error in $d_{m,r}$ measurement.
288 Meanwhile, at the same extent of perturbation in v , the larger size GNR (CTAB-40-850) exhibits
289 a slightly higher CE. This effect is not clear for perturbation in $d_{m,r}$. Still, 0 % to 5 % perturbation
290 in v yields a negligibly small CE ($CE/2 < 6\%$), meaning, on average, $< 6\%$ error in prediction of
291 d_r and L_r . By comparison, a 0 % to 5 % perturbation in $d_{m,r}$ yields a relatively larger error in
292 prediction ($CE/2 < 23\%$), meaning errors in the DMA measurement can potentially translate into
293 significant bias relative to the true value.

294 Finally, the perturbation in adlayer thickness was also examined. In this case, as expected, the
295 larger size GNR (CTAB-40-850) yields a smaller CE with respect to the same extent of
296 perturbation (Figure 4(c)). In other words, as GNR mass/volume increases, the contribution of the
297 relatively thin adlayer decreases.

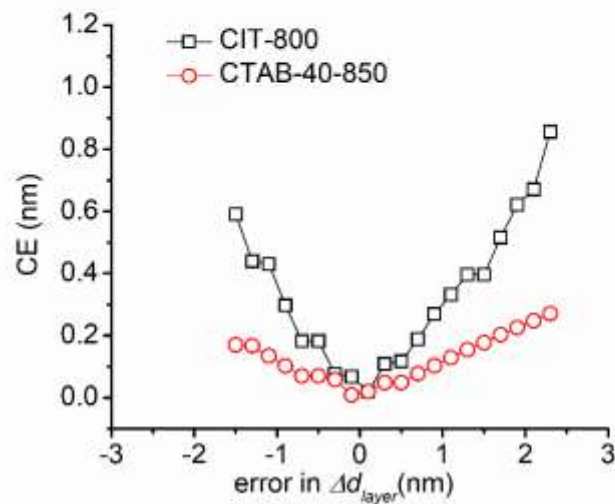
(a)



(b)



(c)

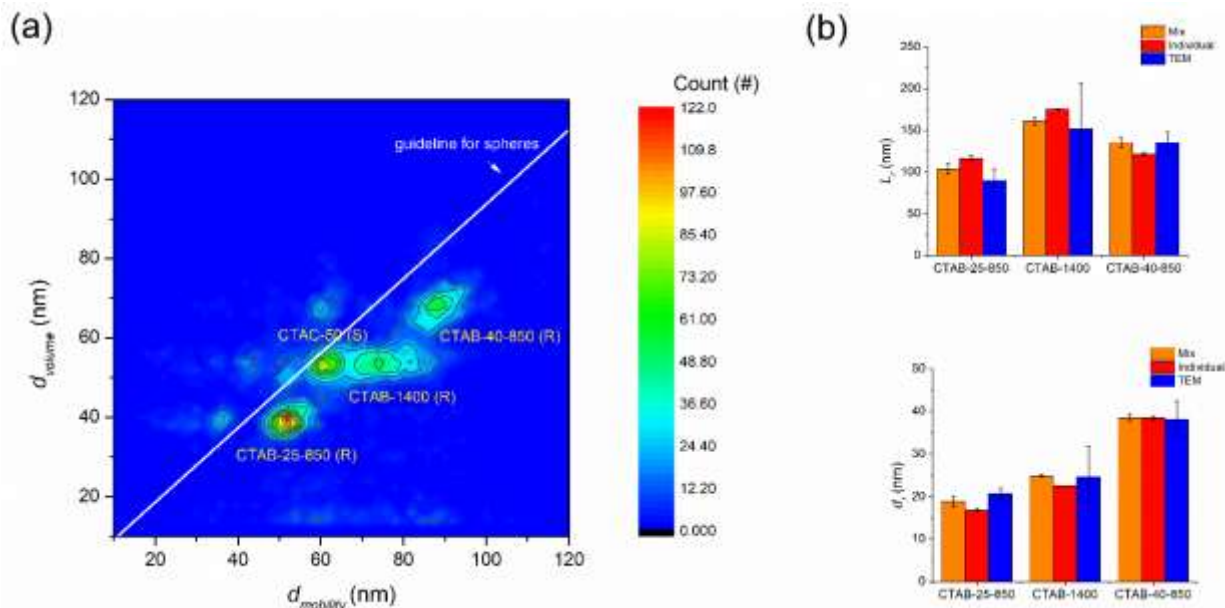


299 Figure 4. Robustness analysis of DMA-spICP-MS method. CE is defined as the combined error as
300 defined in Eq. (5). (a) Change of L_r , d_r , and CE with respect to perturbation in $d_{m,r}$ measurement
301 (CTAB-40-850 as an example). (b) Effect of both $d_{m,r}$ and v perturbation on CE comparing two
302 different dimensional configurations (CIT-800 vs. CTAB-40-850). (c) Effect of adlayer Δd_{layer} on
303 CE comparing two different geometries (CIT-800 vs CTAB-40-850).

304

305 **Nanorod detection and separation based on AR**

306 The quality and purity of synthesized GNRs is essential for critical applications, however
307 polydisperse GNRs with undesired by-products are frequently observed in both laboratory and
308 commercial grade materials. [24,31] From a quality control perspective, applicability of DMA-
309 spICP-MS for such a purpose was investigated by intentionally combining GNRs having different
310 dimensions (i.e., CTAB-20-850, CTAB-40-850 and CTAB-1400) with spheroidal gold NPs
311 (CTAC-50). A contour plot is used to visualize and interpret the data. Prior to the construction of
312 the contour plot, the intensity of GNRs for each spike were converted to volume (and further to
313 diameter) using RM8013 as a calibration standard. Figure 5(a) shows that four populations can be
314 resolved, each representing a specific geometry/size combination. The white line represents the
315 theoretical expectation for spherical nanoparticles, where the volume based diameter d_{vol} should
316 track linearly with the mobility diameter d_m . This line was constructed by linear fit to RM8012 and
317 RM8013, the slope of which is about 0.94, meaning there is inherently a bias in mobility-based
318 diameter versus volume-based diameter. Among the four populations, one lies very close to the
319 white line, which corresponds to CTAC-50 spherical gold NPs. The other populations deviate from
320 the theoretical line, a characteristic associated with non-spherical geometry. Using d_m and d_{vol}
321 from the peak of each population in our model, the d_r and L_r for each GNR are obtainable. The
322 results for determining the GNR dimensions from the mixture are compared with that from
323 individual measurements as well as benchmark TEM values in Figure 5(b). The adlayer thickness
324 was considered in all cases. The d_r and L_r measured from multicomponent mixtures is in good
325 agreement with individual measurements as well as TEM benchmark values, and therefore
326 indicates robustness of the method. The DMA-spICP-MS method can thus distinguish spherical
327 nanoparticles from rods, has sufficient resolution to separate GNRs with different ARs, and yields
328 an accurate dimensional measurement for each population in a mixture.



329
 330
 331 Figure 5 (a) Comparison of volume-based d_{vol} and mobility diameter d_m for a mixture of GNRs
 332 and gold nano-spheres. The heat bar represents the particle counts. (b) L_r , d_r obtained from the
 333 mixture, individual GNRs and the TEM benchmark data.

334
 335 In some cases, there may be no significant adlayer on the ES processed GNRs, while the gas
 336 contribution is relatively small (i.e., $\Delta d_{gas} + \Delta d_{layer} \approx 0$). For example, this may include GNRs
 337 that have no ligand functionalization, GNRs in a cleaner medium, or GNRs that can be dialyzed
 338 into a volatile buffer (such as ammonium acetate) without loss of stability. In this case, a reduced
 339 form combining equations (1)-(2) would be obtained as follows:

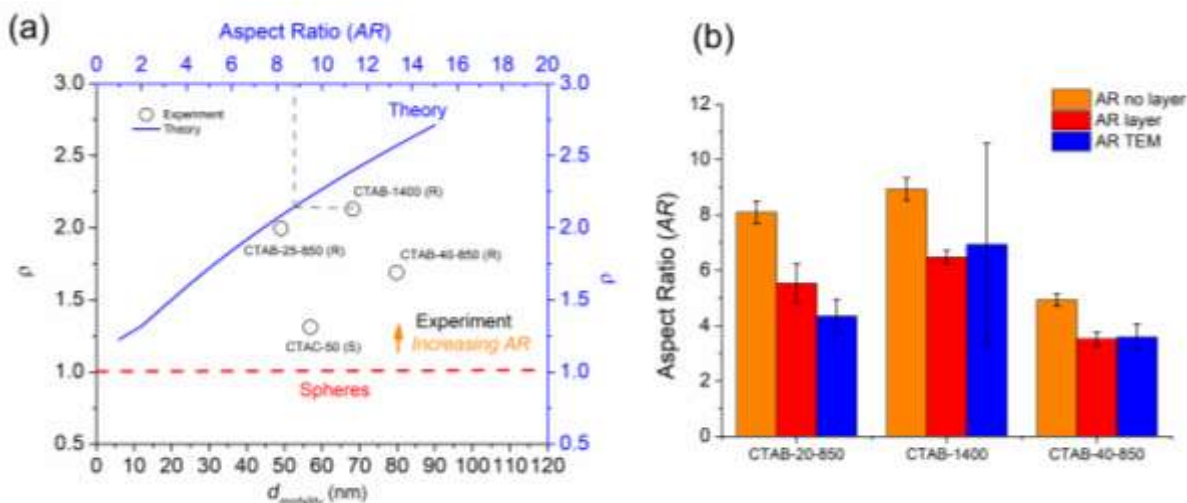
$$340 \quad \rho = \frac{v_m}{v} = \frac{2(AR+0.5)^{1.5}}{3AR}, \quad (6)$$

341 where $\frac{v_m}{v}$ is defined here as a mobility-based apparent density, ρ [19]. Theoretically, for a mixture
 342 of GNRs with different geometries or ARs, one could differentiate between the species using ρ
 343 measured by DMA-spICP-MS or alternatively use ρ to estimate the AR. The GNR samples
 344 examined in this study are not sufficiently stable after removing the solution components, and we
 345 did not have a perfect mixture of clean or non-surface functionalized GNRs available to test this
 346 relationship. Instead, for this purpose, we utilized the same rod mixture and gold nanospheres as
 347 in Figure 5(a), therefore with an expectation of measurable deviation from equation (5). The
 348 different populations have been identified as in Figure 5(a) and the peak value (d_m , d_{vol}) was
 349 utilized to calculate ρ (i.e., $v_m = \frac{\pi}{6} d_m^3$, $v = \frac{\pi}{6} d_{vol}^3$). Each population is represented by open
 350 symbols in Figure 6(a) where ρ vs. d_m is presented. The blue line represents the theoretical
 351 relationship between ρ and AR based on Eq. (6). For each GNR, from the experimentally measured
 352 ρ , its corresponding AR was derived from the blue curve. Briefly, we draw a horizontal line from
 353 the center of the symbol (result) to a point where it intersects the blue line. The x value at that point
 354 is the AR (gray dotted line). The ARs obtained in this manner for the three GNR populations
 355 yielded values of about 8.1, 8.9 and 4.9 (orange bar in Figure 6 (b)). These values correspond to
 356 CTAB-20-850, CTAB-1400 and CTAB-40-850, with TEM benchmark ARs 4.3, 6.9 and 3.6,

357 respectively (blue bar in Figure 6 (b)). The reason for the observed deviation from the true AR is
 358 primarily due to the assumption that $\Delta d_{gas} + \Delta d_{layer} \approx 0$. If the adlayer obtained from TEM
 359 images is considered in the model, the AR obtained from Figure 5(b) using values for “mix”
 360 (orange bar), based on $AR = L_r/d_r$ for the three GNRs, are 5.5, 6.5, and 3.5, for CTAB-20-850,
 361 CTAB-1400 and CTAB-40-850, respectively (red bar in Figure 6(b)). These values are consistent
 362 with the benchmark TEM values.

363 Overall, the AR differentiation within a mixture of GNRs obtained by DMA-spICP-MS
 364 measurement is deemed satisfactory, and we anticipate an improvement in agreement for samples
 365 in a cleaner medium and without the CTAB coating. Because we applied equations for a rod
 366 geometry to the spheroidal CTAC-50 gold NPs, the corresponding data point in Figure 6(a) yields
 367 a predicted AR of 2 (not 1); in this case, AR=2 is consistent with a “quasi-spherical” shape.

368 The slope of the blue curve represents the sensitivity of the DMA-spICP-MS method in
 369 distinguishing GNRs by their AR value. In our case, a variation of AR ranging from 1 to 10, would
 370 result in an apparent density change of roughly 1. This indicates that this method is limited in
 371 sensitivity with respect to AR determination. Regardless, the technique shows promise in its
 372 capacity for separating and distinguishing mixtures of GNRs with different dimensions and AR
 373 values, combined with a low limit of detection ($\approx 10^5$ particles/mL).^[19]



374
 375 Figure 6 (a) Distinguishing mixtures of GNRs and gold spheres by AR. Hollow symbols are
 376 experimental data ($d_{mobility}$ vs. ρ). The blue line represents the theoretical relationship between AR
 377 and ρ , where ρ is unitless based on its definition (i.e. Eq. (6)). (b) Comparison of AR by three
 378 different methods: (1) AR no layer refers to AR derived from the theoretical curve as in (a), with
 379 an assumption of no adlayer. (2) AR layer refers to AR derived from dimensions obtained from
 380 Figure 5(b) (i.e., “mix”, orange bar). (3) AR TEM is calculated from dimensions measured by
 381 TEM.

382

383 Conclusions

384 By combining information obtained from two orthogonal techniques operated in tandem, we have
385 demonstrated the capacity for a novel approach, ES-DMA-spICP-MS, to simultaneously and
386 rapidly quantify both the length and diameter of technologically important nanorods over a wide
387 range of dimensions, and to differentiate rods from spheroidal contaminants. Commercially
388 available gold nanorods were used to evaluate the approach. Trueness and bias were assessed by
389 comparison with direct measurements obtained off-line using TEM imaging. Due to the nature of
390 spICP-MS, this method has the inherent advantages of fast sampling at low particle concentrations.
391 Because of the high resolution associated with DMA, impurities can be distinguished from rods,
392 and rods within an extremely narrow dimensional range (i.e., single mode population) can be
393 selected for analysis by simply varying the applied voltage. A simple rod-based mobility model
394 was presented and assessed. The model also considers the effect of thin coatings (e.g., from
395 surfactants or ligands). The method is limited by high levels of non-volatile solutes, which lead to
396 thick coatings that can significantly impact the rod dimensions and shape. Additionally, the
397 dependence on spICP-MS detection presents limitations with respect to minimum detectable mass
398 and measurable elements (more specifically their stable isotopes); consequently, the method is
399 applicable primarily to metals or metal containing solids. Overall, this new method should prove
400 valuable for rapid statistically-relevant quality assessment in material development and
401 manufacturing control of applicable asymmetric nanomaterials.

402 **Conflicts of interest**

403 There are no conflicts to declare.

404 **Acknowledgements**

405 The authors thank Prof. De-Hao Tsai (National Tsing Hua University, Department of Chemical
406 Engineering) and Kaleb Duelge (NIST/UMD) for critical review and comments on the draft
407 manuscript. JT was supported by a grant from NIST (award #70NANB13H021).

408 **Notes**

409 † The identification of any commercial product or trade name does not imply endorsement or
410 recommendation by National Institute of Standards and Technology.

411 **References**

- 412 1. Y. Li, W. Shen, *Chem Soc Rev*, 2014, **43**, 1543-74.
- 413 2. X. Huang, S. Neretina, M. A. El-Sayed, *Adv Mater*, 2009, **21**, 4880-910.
- 414 3. N. K. Reddy, M. Devika, C. W. Tu, *RSV Adv.*, 2014, **4**, 37563-37568.
- 415 4. A. Manekkathodi, M. Y. Lu, C. W. Wang, L. J. Chen, *Advanced Materials*, 2017, **22**, 4059-4063.
- 416 5. S. Liang, F. Teng, G. Bulgan, R. Zong, Y. Zhu, *J. Phys. Chem.*, 2008, **112**, 5307-5315.
- 417 6. D. Pissuwan, S. Valenzuela, M. B. Cortie, *Biotechnol Genet Eng Rev*, 2008, **25**, 93-112.
- 418 7. J. Cao, T. Sun, K. T. V. Grattan, *Sensors and Actuators B: Chemical*, 2014, **195**, 332-351.
- 419 8. T. B. Huff, L. Tong, Y. Zhao, M. N. Hansen, J. X. Cheng, A. Wei, *Nanomedicine (Lond)*, 2007, **2**, 125-
420 32.
- 421 9. S. Link, M. B. Mohamed, M. A. El-Sayed*, *J. Phys. Chem. B*, 1999, **103**, 3073-3077.
- 422 10. A. Brioude, X. C. Jiang, M. P. Pileni, *J Phys Chem B*, 2005, **109**, 13138-42.

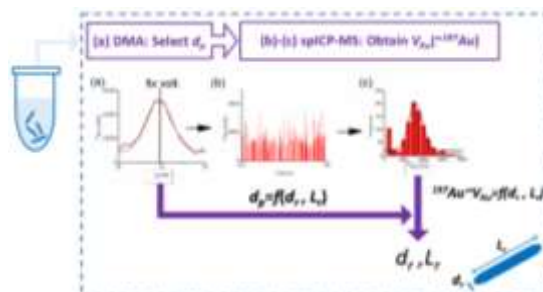
- 423 11. L. S. Slaughter, W.-S. Chang, P. Swanglap, A. Tcherniak, B. P. Khanal, E. R. Zubarev, S. Link, *J. Phys.*
 424 *Chem. C*, 2010, **114**, 4934-4938.
- 425 12. R. D. Near, S. C. Hayden, M. A. El-Sayed, *J. Phys. Chem. C*, 2013, **117**, 18653-18656.
- 426 13. B. N. Khlebtsov, N. G. Khlebtsov, *J. Phys. Chem.*, 2007, **111**, 11516-11527.
- 427 14. N. H. Xu, B. F. Bai, Q. F. Tan, G. F. Jin, *Optics Express*, 2013, **21**, 2987-3000.
- 428 15. B. N. Khlebtsov, V. A. Khanadeev, N. G. Khlebtsov, *J. Phys. Chem. C*, 2008, **112**, 12760-112768.
- 429 16. B. N. Khlebtsov, V. A. Khanadeev, N. G. Khlebtsov, *Phys. Chem. Chem. Phys.*, 2014, **16**, 5710-5722.
- 430 17. Z. J. Hu, S. Hou, Y. L. Ji, T. Wen, W. Q. Liu, H. Zhang, X. W. Shi, J. Yan, X. C. Wu, *AIP Advances*, 2014,
 431 **4**, 117137.
- 432 18. S. Elzey, D. H. Tsai, L. L. Yu, M. R. Winchester, M. E. Kelley, *Anal Bioanal Chem*, 2013, **405**, 2279-
 433 88.
- 434 19. J. Tan, J. Liu, M. Li, H. El Hadri, V. A. Hackley, M. R. Zachariah, *Anal Chem*, 2016, **88**, 8548-55.
- 435 20. S. Guha, M. Li, M. J. Tarlov, M. R. Zachariah, *Trends Biotechnol*, 2012, **30**, 291-300.
- 436 21. S. H. Kim, G. W. Mulholland, M. R. Zachariah, *J. Aerosol Sci.*, 2007, **38**, 823-842.
- 437 22. M. Li, R. You, G. W. Mulholland, M. R. Zachariah, *Aerosol Science and Technology*, 2014, **48**, 22-
 438 30.
- 439 23. M. Li, R. You, G. W. Mulholland, M. R. Zachariah, *Aerosol Science and Technology*, 2013, **47**, 1101-
 440 1107.
- 441 24. T. Nguyen, J. Liu, V. Hackley, *Chromatography*, 2015, **2**, 422-435.
- 442 25. Reference Material 8013, Gold Nanoparticles, Nominal 60 nm Diameter, *National Institute of*
 443 *Standards and Technology*, 2015.
- 444 26. A. Zelenyuk, D. Imre, *Aerosol Science and Technology*, 2007, **41**, 112-124
- 445 27 M. Li, G. W. Mulholland, M. R. Zachariah, *Aerosol Science and Technology*, 2012, **46**, 1035-1044
- 446 28 M. Li, G. W. Mulholland, M. R. Zachariah, *Physical Review E*, 2014, **89**, 022112
- 447 29 B. K. Ku, J. Fernandez de la Mora, *Aerosol Science and Technology*, 2009, **43**, 241-249.
- 448 30. J. Tuoriniemi, G. Cornelis, M. Hasselov, *Analytical Chemistry*, 2012, **84**, 3965-3972.
- 449 31. T. M. Nguyen, J. M. Pettibone, J. Gigault, V. A. Hackley, *Anal Bioanal Chem*, 2016, **408**, 2195-201.

450

451

452

453 TOC



454

455 Fast, quantitative measurement of nanorod dimensions using tandem ion mobility spectrometry-
 456 single particle inductively coupled mass spectrometry.

Electronic Supplementary Information

Fast quantification of nanorod geometry by DMA-spICP-MS

Jiaojie Tan ^{1,2}, Yong Yang², Hind El Hadri¹, Mingdong Li³, Vincent A. Hackley*¹, and Michael R. Zachariah*^{2,3}

1. Materials Measurement Science Division, National Institute of Standards and Technology, Gaithersburg, Maryland 20899, United States
2. University of Maryland, College Park, Maryland 20742, United States.
3. Chemical Sciences Division, National Institute of Standards and Technology, Gaithersburg, Maryland 20899, United States

Table of Contents

Figure S1. Graphical representation of Eq. (1)

Figure S2. TEM image for gold nanorods (GNRs)

Table S1. Dimensions for GNRs provided by vendor (transmission electron microscopy, TEM)

Figure S3. Measurement of layer thickness. Effect of dilution and collection method

Figure S4. Measurement of layer thickness and effect of GNRs sampling number

Figure S5. Contribution of non-volatiles from electrospray (ES) to layer thickness

Table S2: Contribution of non-volatiles from ES to layer thickness (nm)

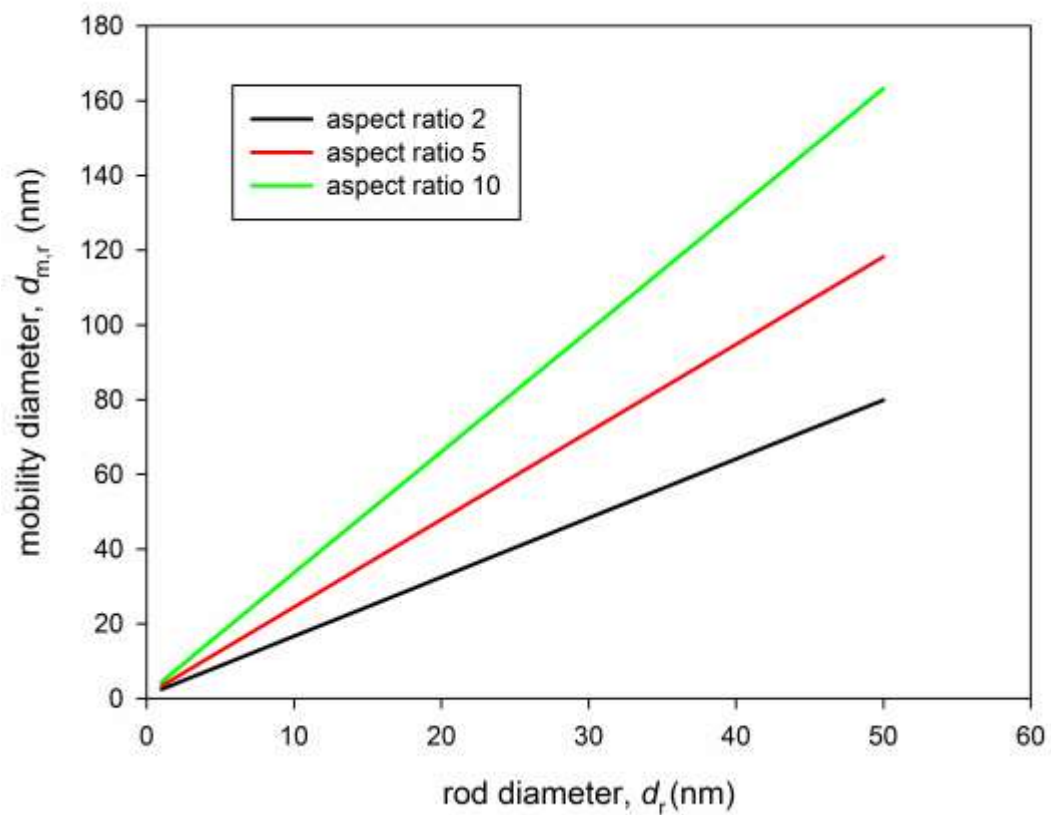


Figure S1. Graphical presentation of Eq. (1) showing the relationship between mobility diameter and rod (cylindrical) diameter as a function of aspect ratio (L_r/d_r) for model rods. $\Delta d_{gas} = 0.68$ nm.

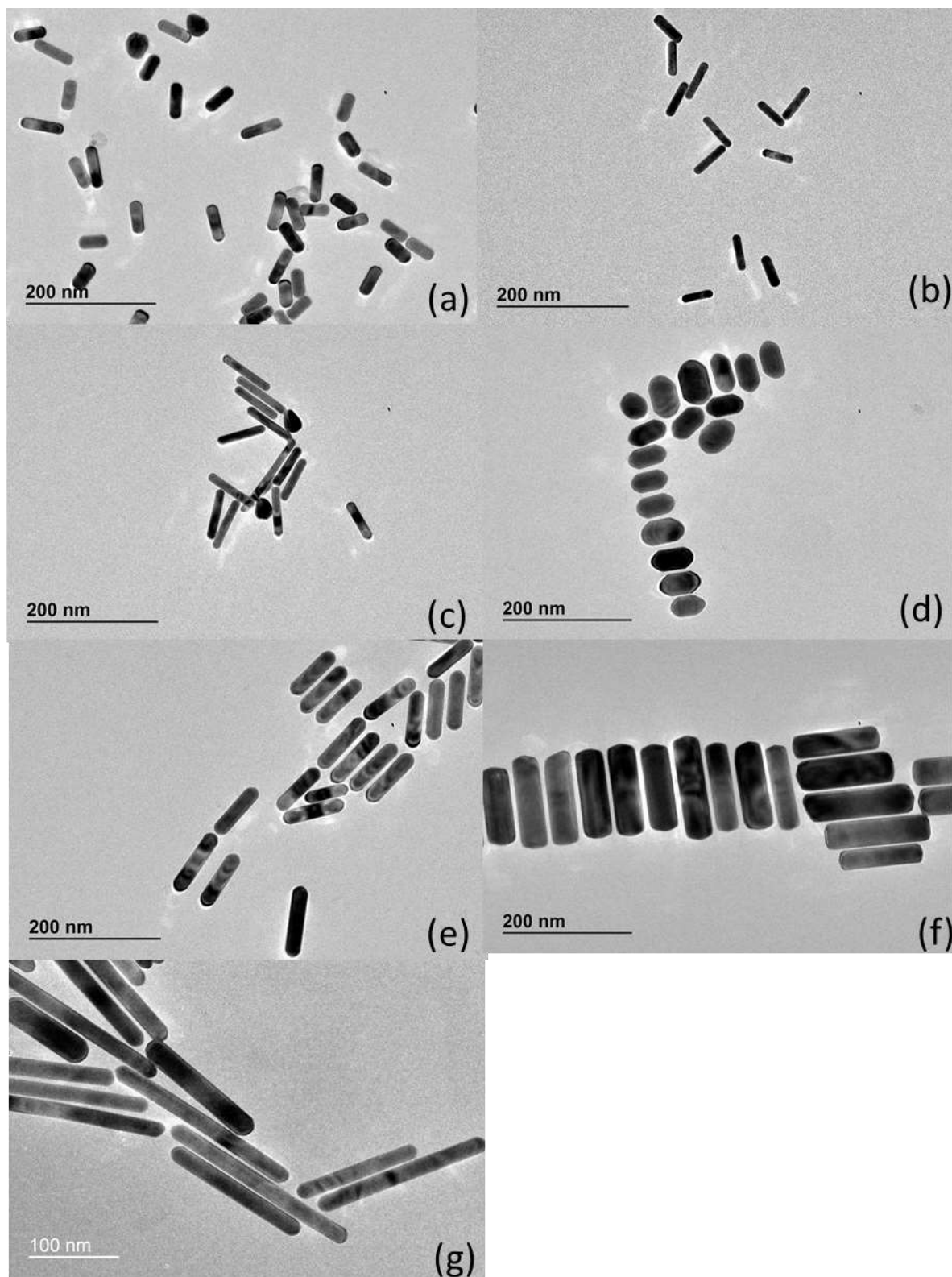


Figure S2. TEM image for GNRs (a) CIT-660 (b) CIT-800 (c) CIT-980 (d) CTAB-600 (e) CTAB-20-850 (f) CTAB-40-850 (g) CTAB-1400

Table S1. Dimensions of GNRs as provided by the vendors (based on TEM) (+/- values represent 1 standard deviation).

GNRs	Diameter (d_r, nm)	Length (L_r, nm)	Aspect Ratio (AR)
CIT-660	17.4 ± 1.2	45.5 ± 6.3	2.6
CIT-800	12.5 ± 1.4	50.8 ± 5.0	4.1
CIT-980	12.1 ± 0.8	69.7 ± 7.3	5.8
CTAB-600	25	57	2.3
CTAB-20-850	23	89	3.9
CTAB-40-850	44	160	3.6
CTAB-1400	25	256	10.2

Estimating Adlayer Thickness on GNRs

To estimate the mean adlayer thickness on GNRs, approximately 10 GNRs were analyzed by TEM for each sample and using different locations on the grid within a single GNR sample. For the case where thickness was non-uniform, different locations were randomly selected along the GNR and averaged. Figure S2 shows the effect of sample dilution and collection method on results. A relatively large standard deviation for adlayer thickness was observed as represented in Figures S2 and S3. The reason for the large variation in thickness is not clearly understood. It is presumed to be the result of the manufacturing process and partially due to non-uniformities in the electrospray droplets and non-uniform drying process along the rod, which yields non-uniform non-volatile layer thickness (Figure S4).

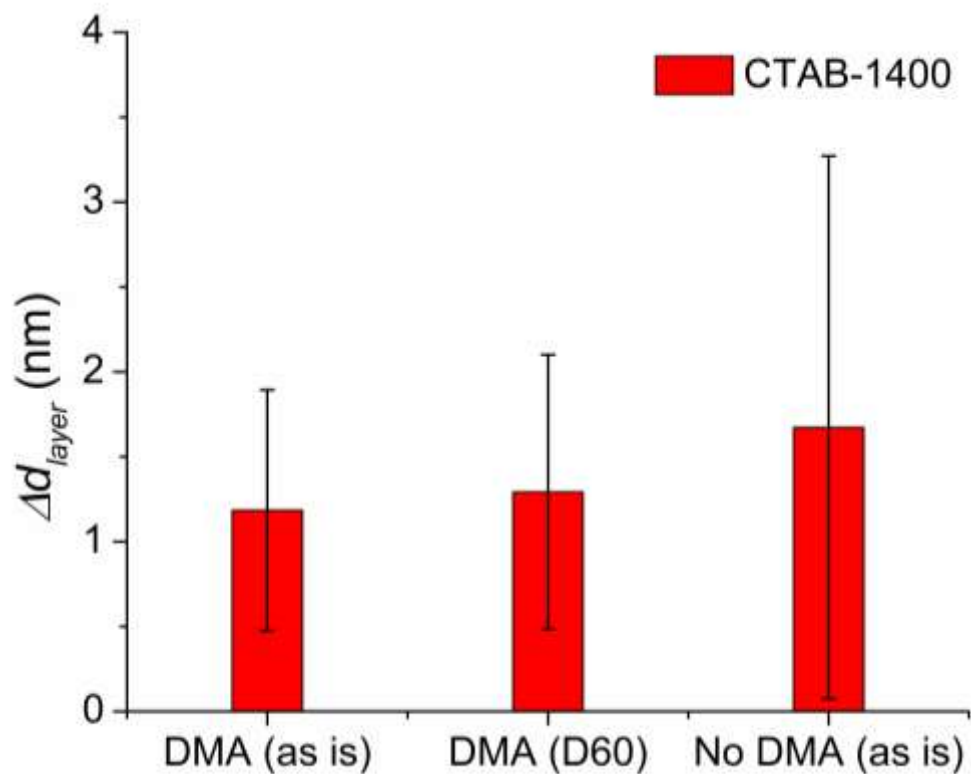


Figure S3. Measurement of adlayer thickness showing the effect of dilution and collection method. D60 indicates 60× dilution compared with the native suspension. The adlayer thickness observed with DMA size selection is compared with that without DMA selection. Neither the effect of dilution nor DMA selection has an obvious effect on adlayer thickness. Roughly 10 GNRs and multiple locations along each GNR were measured to yield an average and one standard deviation.

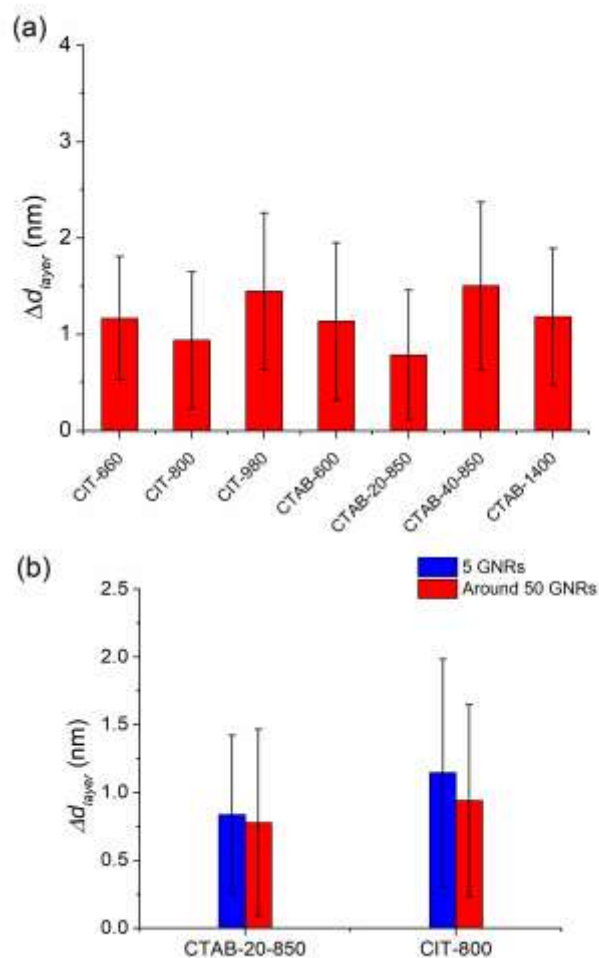


Figure S4. Measurement of adlayer thickness and effect of GNR sampling number. (a) Adlayer thickness of all GNR samples by TEM imaging of electrostatically deposited GNRs at peak size selected by DMA and based on the analysis of 10 GNRs per sample. (b) Comparison of number of GNRs randomly sampled (5 vs. roughly 50) on the determination of layer thickness for both CTAB and CIT coated samples. Multiple locations along each GNR were measured to obtain the average and one standard deviation. Results indicate that the adlayer thickness estimated from 10 GNRs is statistically representative of the larger population (compared to the inherent variations in adlayer thickness present).

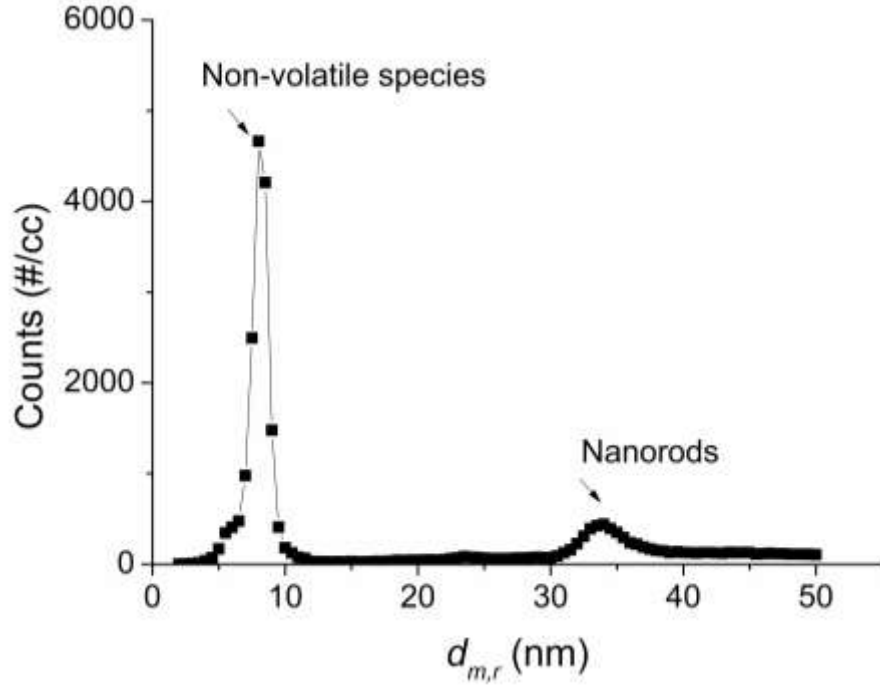


Figure S5. Contribution of non-volatiles from ES to the adlayer thickness. Mobility size distribution of CIT-600 by ES-DMA-CPC (CPC is a condensation particle counter).

The peak at 8 nm is representative of dried particles containing non-volatile species, while the peak at 34 nm is representative of GNRs. The volume of the non-volatile species can be estimated by $d_{m,r}^3$. This same volume of non-volatile species will form an adlayer thickness (Δr) on the GNR surface with radius of r and length of L . These parameters follow from Eq. (1):

$$\frac{\pi}{6} d_{m,r}^3 = \pi(r + \Delta r)^2 L - \pi r^2 = \pi \Delta r^2 L + 2\pi r \Delta r L . \quad (1)$$

The contribution of non-volatiles from ES (i.e., Δr) was calculated based on Eq. (1).

Table S2: Contribution of non-volatiles from ES to layer thickness (nm)

GNRs	Contribution from ES to adlayer thickness (nm)
CIT-660	0.2
CIT-800	2.2
CIT-980	0.1
CTAB-600	1.1
CTAB-20-850	0.1
CTAB-40-850	0.1
CTAB-1400	0.3